Mechanical Systems and Signal Processing 235 (2025) 112777

Contents lists available at ScienceDirect

Mechanical Systems and Signal Processing

journal homepage: www.elsevier.com/locate/ymssp

A novel Doppler-based phase unwrapping algorithm for mmWave MIMO radars and its application to displacement estimation in structural health monitoring

Giorgio Guerzoni [a], Elahe Faghand [a,b], Loris Vincenzi [a,*], Elisa Bassoli [a], Giorgio Matteo Vitetta [a]

[a] Department of Engineering 'Enzo Ferrari', University of Modena e Reggio Emilia, Modena, Italy
[b] Department of Electrical Engineering, Shahid Beheshti University, Tehran, Iran

ARTICLE INFO

Communicated by Z. Mao

Keywords:
MIMO radar
Displacement measurement
Phase wrapping
Doppler
Structural health monitoring

ABSTRACT

In this manuscript, the problem of estimating dynamic structural displacements through mmWave multiple-input multiple-output frequency modulated continuous wave radars is investigated. These devices allow to potentially achieve high accuracy in the measurement of radial displacements. However, in the presence of moving targets, their resolution is affected by the phase wrapping phenomenon; this occurs when, in the time interval separating consecutive measurements, the target to be tracked moves by more than a quarter of the radar wavelength. To mitigate this problem, a novel iterative method for performing phase unwrapping on the basis of estimated Doppler information is developed. Our experimental results evidence that the proposed method can be exploited to faithfully reconstruct the phase trajectory associated with specific points of quickly moving objects and, consequently, to carefully estimate their radial displacement also in those scenarios where traditional techniques are bound to fail, at the price of a small computational complexity.

1. Introduction

Nowadays, a fundamental role in civil engineering is played by *structural health monitoring* (SHM) systems, since these allow to detect potential areas of structural weakness in the built environment at an early stage. Such systems usually exploit multiple sensors to acquire displacement information about the monitored structures in dynamic conditions; this is due to the fact that such information are directly correlated with structural integrity and provide valuable insights into various technical issues (e.g., system identification, model updating and earthquake engineering).

Different methods can be adopted for the measurements of dynamic structural displacements. On the one hand, *direct* methods process measurements acquired through sensors that can directly provide displacement information. Sensors of this type include *linear voltage displacement transducers* (LVDTs), *laser doppler vibrometers* (LDVs) [1,2], vision cameras [3], *global navigation satellite system* (GNSS) receivers [4] and ground-based radars. On the other hand, *indirect* methods exploit sensors (like accelerometers [5] and strain gauges), whose measurements can be converted to displacement information [6]. However, in the last case, the extraction of accurate displacement information from the available measurements may represent a challenging task and entail significant errors. Moreover, the use of contact sensors, such as accelerometers, strain gauges, or LVDTs, is not always possible. In fact, first of all,

* Corresponding author.
E-mail address: loris.vincenzi@unimore.it (L. Vincenzi).

https://doi.org/10.1016/j.ymssp.2025.112777
Received 10 May 2024; Received in revised form 22 March 2025; Accepted 18 April 2025
Available online 6 June 2025

sensors directly providing displacement information (e.g., LVDTs) require a fixed measurement base, often unavailable in field conditions. In addition, contact sensors may potentially interfere with the functionality of the monitored structure, may require complex wiring and installation processes, and entail significant costs, especially when monitoring multiple points.

Non-contact systems may also suffer from various limitations. For instance, vision cameras and LDV can be affected by environmental conditions, whereas GNSS systems are limited by their centimetre-level accuracy [4]. Structural monitoring based on satellite radar data is gaining increasing attention thanks to its capability to oversee structures and infrastructures on a broad territorial scale [7]. Nonetheless, its applicability is limited to the quasi-static monitoring of structures and infrastructures, as the periodicity of data acquisition is quite long. Most of the above mentioned limitations can be overcome through the use of ground-based radar sensing [8]. In fact, radar sensing is contactless, is unaffected by environmental conditions and is capable of directly measuring displacements in both quasi-static and dynamic conditions. Most of the manuscripts available in the technical literature about the use of radar technology in SHM of the built environment mainly concern the exploitation of *real aperture radar* (RAR) and *synthetic aperture radar* (SAR) systems for displacement-based dynamic monitoring. On the one hand, RAR systems have been shown to be effective in the monitoring of tall and flexible structures (e.g., see [9,10]), but achieve limited accuracy when these exhibit high fundamental frequencies [11]. On the other hand, SAR systems are usually unsuitable for structural dynamic monitoring because of their limited scanning speed [4,12].

Recently, in the field of radar-based SHM, various research efforts have focused on the use of: a) microwave interferometric radars; b) colocated[1] radar devices equipped with multiple *transmit* (TX) and *receive* (RX) antennas (i.e., of *multiple-input multiple-output*, MIMO, type), and operating at *millimeter-wave* (mmWave) [13–15]. This interest can be motivated as follows. High speed microwave interferometry has been shown to be a viable option for both static and dynamic testing of structures and infrastructures [16,17]. The interferometric radars considered in the technical literature operate in the microwave spectrum and are equipped with a limited number of antennas. Although a working frequency in the GHz range allows to achieve millimeter-level accuracy in the estimation of radial displacements, the use of a limited number of antennas limits the angular resolution of such radar systems [18]. Colocated MIMO radars operating at mmWave, instead, are able to detect sub-millimeter displacements and, if equipped with large antenna arrays, can monitor multiple points of the monitored structure. In recent years, colocated MIMO radars of *Frequency-Modulated Continuous Wave* (FMCW) type, endowed with a large number of antennas, and operating at 24, 60 or 77 GHz have become available at a fraction of the cost of previous technologies. Thanks to their features, they have become the elected choice for researchers, and their use cases have far outreached the automotive field [19,20], reaching SHM too [21]. Being their wavelength in the order of a few millimeters, they allow to achieve a substantially better resolution in radial displacement (down to a few hundredth of a millimeter). On the other hand, this makes the so called *phase wrapping* problem severe and difficult to avoid. Phase wrapping is a phenomenon that occurs when the object to be tracked moves by more than a quarter wavelength during the time interval separating two consecutive measurements. In this case, the total round trip length experienced by the electromagnetic wave radiated by the radar device exceeds half a wavelength; this results in a phase rotation greater than π radians in the corresponding electromagnetic echo detected at the RX side. When this happens, the object displacement cannot be unambiguously estimated on the basis of the phase rotation alone.

Various methods have been proposed in the technical literature to solve the phase wrapping problem, although not all are suitable for structural monitoring applications [22–27]. More specifically, a linear interferometric method, based on linear phase demodulation technique initially designed for *continuous wave* (CW) and then adapted to FMCW radars, has been developed for measuring large displacements in [23,28]; however, the maximum inter-fame displacement is limited to one fourth the wavelength of the radiated signal. An adaptive phase unwrapping algorithm aided by acceleration has been illustrated in [29] to keep track of displacement when the line of sight with the radar is interrupted by an obstructing object for a brief period of time; the main drawback of this solution is represented by the needs of supplementary hardware. An alternative to the above mentioned solutions is offered by the techniques developed in [22,25] for the estimation of small displacements and based on the so called *Viterbi algorithm* for the mitigation of the effects of noise in phase unwrapping. Unluckily, they are not suitable to SHM applications where both small and large displacements occurring at high velocity need to be tracked.

A conceptually different approach to phase unwrapping is pursued in [24,26,27], where machine learning techniques are exploited to tackle it. However, the solutions illustrated in those manuscripts have been devised for entire SAR images and cannot be adapted to mmWave MIMO radars, which can be used to independently track the displacement of individual points; note that this represents a crucial aspect in SHM applications, where detecting local damages, potentially leading to local displacements and deformations different from those appearing in the other parts of the considered structure, is one of the main goals.

In this manuscript, a novel iterative method for performing phase unwrapping in a colocated MIMO FMCW radar is illustrated. The proposed method has the following relevant features:

(1) It exploits Doppler information to predict the phase of the received signal at future time instants, and then exploit a phase measurement to correct this prediction, even when the phase rotates by tens of radians between two subsequent radar frames.

(2) It allows to track the phase variations characterizing specific points of a radar image, without exploiting the possible correlations between spatially close points.

(3) It is computationally simple and does not the require the use of additional sensors (e.g., an accelerometer).

The accuracy of our method has been assessed on the basis of the measurements acquired in a controlled laboratory environment and in the monitoring of a real footbridge. Our numerical results evidence that our method is able to track the target phase (and,

[1] The term *colocated* means that the transmit and receive arrays of the radar are close to each other, usually on the same board, and that the radar size is small with respect to its range resolution.

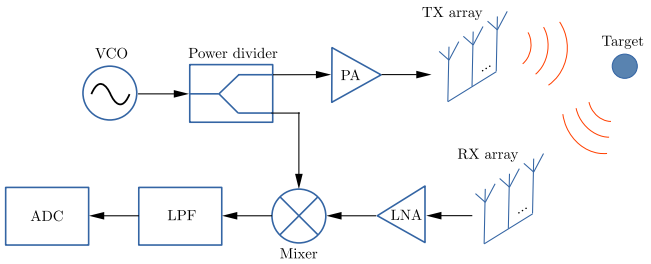

Fig. 1. FMCW radar block diagram of a colocated MIMO FMCW radar system.

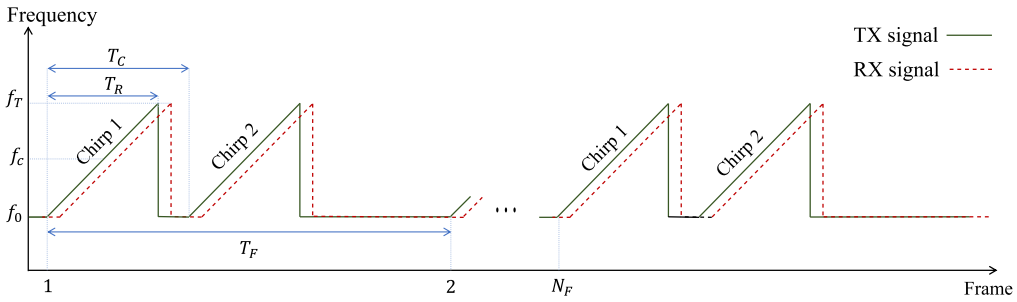

Fig. 2. Time evolution of the instantaneous frequency of the oscillation generated by the VCO block appearing in Fig. 1. In this case each frame contains two chirps (i.e., $N_c = 2$). Usually, for commercial devices, T_F is tens of times greater than T_C.

thus, the displacement) and, in particular, to resolve the phase ambiguity even when the phase jump between two consecutive radar frames is as wide as 10π radians.

The remaining part of this manuscript is organized as follows. The architecture of a MIMO FMCW radar and various related signal models are illustrated in Section 2. The phase wrapping problem and a simple solution to it are described in Section 3. Our phase unwrapping algorithm is developed in Section 4, whereas its performance is analyzed in Section 5. Finally, some conclusions are offered in Section 6.

2. System and signal models

In this section the architecture of a colocated FMCW MIMO radar equipped with N_T TX antennas and N_R RX antennas is analyzed[2]; in our description we refer to the block diagram illustrated in Fig. 1, that describes the signal processing tasks executed at both TX and RX sides.

At the TX side, a *voltage controlled oscillator* (VCO) is employed to generate a frequency modulated wave, whose instantaneous frequency evolves according to the periodic pattern shown in Fig. 2. As it can be easily inferred from that figure, the transmission is organized in *frames*, each encompassing N_c consecutive *chirp* signals, characterized by an instantaneous frequency increasing linearly over time. Note also that: a) each chirp lasts T_R s; b) the interval separating the start of two consecutive chirps within the same frame lasts T_C s; c) the interval separating the start of two consecutive frames lasts T_F s.

Let us analyze the signal $s^{(\mathrm{VCO})}(t)$ generated during each chirp interval. In particular, we consider, for simplicity, the chirp signal generated during the interval $[0, T_R)$ (see Fig. 2); this signal can be expressed as

$$s^{(\mathrm{VCO})}(t) = V_0 \exp\left(j2\pi\left(f_0 + \mu t\right) t\right), \tag{1}$$

where V_0 is the signal amplitude, μ is the chirp slope and f_0 is the start frequency. Note that the lowest and the highest frequencies generated during each chirp are f_0 and

$$f_T = f_0 + \mu T_R, \tag{2}$$

respectively, so that the *central frequency* is

$$f_c = \frac{f_T + f_0}{2}. \tag{3}$$

Given f_c, the radar wavelength λ can be computed as c/f_c, where c is the speed of light.

[2] The presence of non-idealities is ignored here, for simplicity; however, in practice, these need to be carefully compensated for in order to mitigate their impact on estimation accuracy (e.g., see [30] and references therein).

The VCO output signal $s^{(\mathrm{VCO})}(t)$ is applied to a power divider feeding both a *power amplifier* (PA) and the local oscillator port of a mixer. The PA raises the power level of the VCO signal before sending it to one of the antenna elements of the available TX array. The radiated signal $s^{(\mathrm{TX})}(t)$ can be expressed as

$$s^{(\mathrm{TX})}(t) = A\Re\{s^{(\mathrm{VCO})}(t)\}, \tag{4}$$

where $\Re\{x\}$ denotes the real part of x and A is real positive parameter accounting for power amplification.

Let us assume now that the VCO signal is radiated by a single TX antenna (namely, the n_Tth TX antenna, with $n_T \in \{1, 2, \ldots, N_T\}$) and, then, it is reflected by a single *point target*. The electromagnetic echo generated by that target is received by each antenna of the RX array; for this reason, N_R signals become available at the output of that array when a single TX antenna is activated. To simplify our mathematical description of the received signals, it is useful to refer to the *virtual array* associated with the given TX and RX *physical arrays*. This array is obtained replacing each couple of TX and RX physical antennas with a single virtual element located in the median position of the considered antenna pair.[3] Therefore, in principle, the considered radar system is equipped with a virtual array consisting of $N_T N_R$ virtual antennas. Actually, some of the virtual antennas may overlap; in this case, only one of the overlapping elements is arbitrarily selected, so that the overall size N_{VA} of the virtual array is smaller than $N_T N_R$. The construction of the virtual array associated with given TX and RX arrays is exemplified by Fig. 3-a), that refers to a case in which $N_T = 2$ and $N_R = 4$. Note that the resulting virtual array, that consists of $N_{VA} = 8$ virtual elements (since there is no overlapping in the generation of the virtual antennas), is characterized by a *linear* geometry, and that the spacing between its adjacent elements is *uniform* and equal to $\lambda/4$ (in other words, the virtual array is a *uniform linear array*, ULA, with $\lambda/4$ inter-antenna spacing). In the following, it is assumed that, for simplicity, the virtual array of the considered radar system is an horizontal ULA, consisting of N_{VA} distinct elements and characterized by a $\lambda/4$ inter-antenna spacing, as shown in Fig. 3-b). Then, If noise and attenuation are ignored, the signal received by the υth virtual element of that array can be expressed as

$$s_\upsilon^{(\mathrm{RX})}(t) = s^{(\mathrm{VCO})}\left(t - \tau_\upsilon\right), \tag{5}$$

with $\upsilon = 1, 2, \ldots, N_{VA}$; here

$$\tau_\upsilon = 2\frac{R_\upsilon}{c} \tag{6}$$

is the *round trip delay* and R_υ is the (unknown) distance between the given pointwise target and the considered virtual element (i.e., the target *range* observed by the considered virtual antenna). The signal $s_\upsilon^{(\mathrm{RX})}(t)$ (5) is applied to a *low noise amplifier* (LNA), raising its power level. The LNA feeds the *radio frequency* (RF) port of the mixer, whose output is sent to a *low pass filter* (LPF). The LPF output can be expressed as (e.g., [31, Eq. (5)])

$$s_\upsilon^{(\mathrm{B})}(t) \simeq \exp\left(j\left(2\pi f_\upsilon^{(\mathrm{B})} t + \phi_\upsilon^{(\mathrm{B})}\right)\right), \tag{7}$$

where

$$f_\upsilon^{(\mathrm{B})} \triangleq \mu\tau_\upsilon \tag{8}$$

is the *beat frequency* and

$$\phi_\upsilon^{(\mathrm{B})} \triangleq 2\pi f_0 \tau_\upsilon \tag{9}$$

is the phase characterizing $s_\upsilon^{(\mathrm{B})}(t)$ (7). Note that both $f_\upsilon^{(\mathrm{B})}$ (8) and $\phi_\upsilon^{(\mathrm{B})}$ (9) are proportional to τ_υ and, consequently, to the target range R_υ (see (6)). However, $f_\upsilon^{(\mathrm{B})}$ can take on an arbitrary value, whereas $\phi_\upsilon^{(\mathrm{B})}$ belongs to the interval $\mathcal{I}_\phi \triangleq [-\pi, \pi)$. This explains why $\phi_\upsilon^{(\mathrm{B})}$ can be exploited at the RX side to measure range variations only if their absolute value does not exceed $\lambda/2$.

Finally, the LPF output $s_\upsilon^{(\mathrm{B})}(t)$ (7) undergoes digitization; the last task is accomplished by an *analog-to-digital converter* (ADC) operating at the sampling frequency $f_s = 1/T_s$, where T_s denotes the sampling period. In each chirp interval, N samples are acquired from each virtual element, with $N \leq T_R/T_s$. The time domain samples acquired in the same chirp interval from the N_{VA} antennas are collected in the $N \times N_{VA}$ complex matrix denoted $\mathbf{S}_\mathrm{T}$; more specifically, the ordered samples originating from the υth virtual antenna (see Fig. 3-b)) form the υth column of $\mathbf{S}_\mathrm{T}$. Once the matrix $\mathbf{S}_\mathrm{T}$ has been generated, the detection of targets, and the estimation of their range and azimuth is accomplished as follows. First of all, *zero padding* (ZP) is applied to all the columns of $\mathbf{S}_\mathrm{T}$ by appending $(N_0^{(\mathrm{R})} - N)$ zeros to each of them.[4] Then, an order $N_0^{(\mathrm{R})}$ *fast Fourier transform* FFT is performed on each column of the resulting zero-padded matrix; this produces the $N_0^{(\mathrm{R})} \times N$ matrix $\mathbf{S}_\mathrm{R}$, that can be easily exploited to detect targets and estimate their range. In fact, if a target is in the field of view of the radar at a range $\bar{R}$, an amplitude peak appears on all the columns of $\mathbf{S}_\mathrm{R}$ and value $\bar{l}$ of the column index identifying this peak is the same for all the columns. This is due to the fact that distinct rows of $\mathbf{S}_\mathrm{R}$ correspond to different values of target range; in particular, the $\bar{l}$th row is associated with the range[5]

$$\bar{R} = (\bar{l} - 1)\frac{c}{2T_s N_0^{(\mathrm{R})}\mu}. \tag{10}$$

[3] The usefulness of this approach is due to the fact that each virtual element can be considered as the antenna of a monostatic radar (i.e., as an antenna employed for both transmission and reception).

[4] Consequently, the size of each column becomes $N_0^{(\mathrm{R})}$

[5] Keep in mind that the use of an order $N_0^{(\mathrm{R})}$ FFT entails range discretization. In fact, the range domain is partitioned into $N_0^{(\mathrm{R})}$ spatial *bins*, each associated with a specific value of the index of the FFT output.

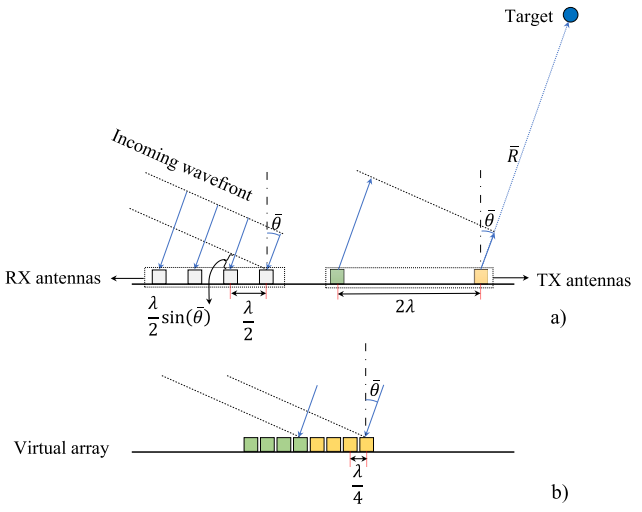

Fig. 3. (a) Physical geometry and b) virtual array of a colocated FMCW MIMO radar equipped with two TX antennas and four RX antennas.

In the presence of multiple targets, the superposition principle can be applied; for this reason, if the target ranges are different, multiple peaks appear along each column of $\mathbf{S}_{\mathrm{R}}$. This is exemplified by Figs. 4-a) and -b) that represent, through color maps, the amplitude of the elements of the matrices $\mathbf{S}_{\mathrm{T}}$ and $\mathbf{S}_{\mathrm{R}}$ in the presence of a couple of point targets, one characterized by the range $R_1 = 4$ m and the azimuth $\theta_1 = -30°$, the other one by the range $R_2 = 10$ m and the azimuth $\theta_2 = 8.5°$; in this simulation, $N = N_0^{(\mathrm{R})} = 128$, $N_{VA} = N_0^{(\mathrm{A})} = 80$, $f_s = 12.8$ MHz, $\mu = 30$ MHz/μs. As it can easily be inferred from Fig. 4-b), the presence of two targets results in two local peaks along each of the columns of $\mathbf{S}_{\mathrm{R}}$. It is important to mention that the range resolution ΔR of an FMCW radar system, i.e. its ability to distinguish two closely spaced targets, can be expressed as

$$\Delta R = \frac{c}{2B}, \tag{11}$$

where $B \triangleq f_T - f_0$ is the bandwidth of the RF signal generated by the VCO. If the difference between the ranges of two point targets is less than ΔR, the peaks originating from such targets will overlap in the same range bin, so that the radar system will not be able to distinguish them in the range domain; this form of mutual interference represents a source of error in range and displacement estimation, and can be mitigated by increasing the radar bandwidth (i.e., by increasing the slope μ or the ramp duration T_R, and adjusting N and/or f_s accordingly). Moreover, the maximum distance $\bar{R}_{max}$ at which a target can be detected is given by

$$\bar{R}_{max} = \frac{c}{\mu}\frac{f_s}{2}. \tag{12}$$

The availability of an horizontal ULA in the considered radar system allows us not only to detect a target and estimate its range, but also to estimate its azimuth (i.e., the *angle of arrival*, AoA, of its electromagnetic echo). This result is achieved by:

(a) Applying ZP to all the rows of $\mathbf{S}_{\mathrm{R}}$; this produces a $N_0^{(\mathrm{R})} \times N_0^{(\mathrm{A})}$ matrix, where $N_0^{(\mathrm{A})} \triangleq N M_A$ and M_A is the adopted *oversampling factor*.

(b) Applying a $N_0^{(\mathrm{A})}$ order FFT to all the rows of the resulting zero-padded matrix.[6]. This produces the $N_0^{(\mathrm{R})} \times N_0^{(\mathrm{A})}$ complex matrix $\mathbf{S}_{\mathrm{A}} = [a_{l,m}]$.

(c) Finding the amplitude peak in the set of elements of $\mathbf{S}_{\mathrm{A}}$. In fact, it can be shown that, in the presence of a single point target characterized by the range $\bar{R} < \bar{R}_{max}$ (Eq. (10)) and the azimuth $\bar{\theta} \in (-90°, 90°)$, an amplitude peak is found at the element $a_{\bar{l},\bar{m}}$ of $\mathbf{S}_{\mathrm{A}}$ identified by the row index $\bar{l}$ and the column index $\bar{m}$; here, $\bar{l}$ is the same index appearing in Eq. (10), whereas

$$\bar{m} \approx \frac{N_0^{(A)}}{2}\sin(\bar{\theta}) + 1. \tag{13}$$

Similarly, in the presence of multiple and adequately spaced targets, multiple peaks will appear in the matrix $\mathbf{S}_{\mathrm{A}}$. This is exemplified by Fig. 4-c), that refers to the case of two targets. Moreover, if two targets have similar angular coordinates, the only way to discriminate them is to use a radar with a larger number of virtual elements N_{VA}. Note that the above mentioned complex quantity $a_{\bar{l},\bar{m}}$ plays an important role in the following, since its amplitude is proportional to the energy returned by the specific spatial region in which a target is detected and its phase can be taken as an estimate of the phase $\phi_v^{(\mathrm{B})}$ (9).

[6] Just like the range FFT, the angular FFT involves the discretization of AoA, but in a nonuniform grid due to the presence of the nonlinear function $\sin(\cdot)$ in (13)

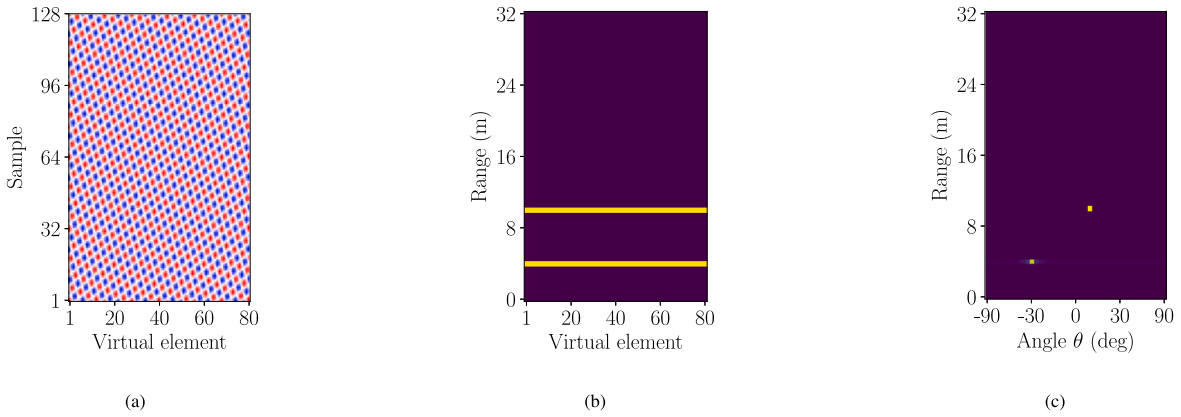

Fig. 4. Representation of the absolute values of the elements of: (a) the matrix $\mathbf{S}_{\mathrm{T}}$, collecting the real part of the samples captured by the ADC ; (b) the corresponding matrix $\mathbf{S}_{\mathrm{R}}$; (c) the corresponding matrix $\mathbf{S}_{\mathrm{A}}$. The presence of two distinct targets is assumed.

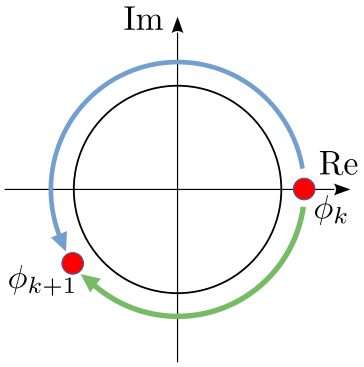

Fig. 5. Representation of the phase wrapping problem. A positive phase variation is misinterpreted as a negative one, since it exceeds π.

3. The phase wrapping problem and the traditional solution to it

Let us analyze now the phase wrapping problem and illustrate the most known solution to it, dubbed *traditional phase unwrapping* (TPU) in the following and widely used in the technical literature [32]. In our description of that problem and its solution we assume that: a) a single chirp is radiated during the transmission of each frame; b) a single point target is present in the radar field of view; c) the target is detected thanks to an amplitude peak located in the $\bar{l}$th row and $\bar{m}$th column of the matrix $\mathbf{S}_{\mathrm{A}}$. If in the time interval separating two consecutive frames the target range changes by $\Delta x \ll \Delta R$ (i.e., the value of $\bar{l}$ does not change; see (10)), the variation experienced by the phase of the element $a_{\bar{l},\bar{m}} \in \mathbf{S}_{\mathrm{A}}$ within two frames is

$$\Delta\phi = \frac{4\pi}{\lambda}\Delta x, \tag{14}$$

as it can be easily inferred from (6) and (9), whereas the index $\bar{l}$ associated with the estimate $\bar{R}$ (10) of the target range does not change at all. For instance, if the central frequency f_c (see (3)) is equal to 77 GHz (so that $\lambda \approx 4$ mm), a range variation of 1 mm will result in a phase variation $\Delta\phi$ approximately equal to π radians. This suggests that, on the one hand, small radial displacements of a given target can be tracked by analyzing the sequence $\{\phi_k; k = 1, 2, \ldots\}$, that collects the phases observed on the same element of $\mathbf{S}_{\mathrm{A}}$ over multiple consecutive frames (here, ϕ_k denotes the phase observed in the kth frame). On the other hand, this idea suffers from an important limitation, since the signal phase is always assumed to belong to the interval $\mathcal{I}_\phi$; this means that any phase variation falling out of this interval leads to a wrong estimate of the displacement. This problem is exemplified by Fig. 5, where the positive variation $(\phi_{k+1} - \phi_k)$ is interpreted as a negative one because it exceeds the upper limit of $\mathcal{I}_\phi$. The existence of the phase wrapping problem implies that the maximum displacement Δx that can be unambiguously detected is limited to $\lambda/4$ (see (14)). In the situation illustrated in Fig. 5, a radial movement *away* from the radar longer than $\lambda/4$ (blue path) is misinterpreted as a movement *toward* the radar (green path) shorter than $\lambda/4$.

If we assume that the absolute value of the phase variation referring to each couple of consecutive elements of the sequence $\{\phi_k; k = 1, 2, \ldots\}$ never exceeds π, unambiguous estimates of the radial displacements with respect to an initial position (associated withe the first phase ϕ_1) can be evaluated through the above mentioned TPU algorithm. This algorithm is fed by the phase sequence $\{\phi_k; k = 1, 2, \ldots\}$ and generates the new sequence $\{\psi_k; k = 1, 2, \ldots\}$, collecting the *unwrapped* signal phases. It is initialized setting

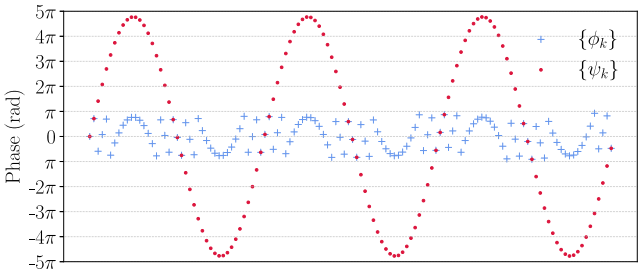

Fig. 6. Representation of a specific phase sequence $\{\phi_k\}$ feeding TPU algorithm and of the corresponding output $\{\psi_k\}$.

$\psi_1 = \phi_1$ and computes ψ_k on the basis of ψ_{k-1} and ϕ_k only for any $k > 1$; more specifically, ψ_k is evaluated by adding to ϕ_k the quantity $2\pi\beta_k$, where β_k is the only relative integer ensuring that $|\psi_k - \psi_{k-1}|$ is smaller than π (see Fig. 6). This procedure can be formalized as in Algorithm 1, where $\lfloor\cdot\rfloor$ denotes the *floor* function. The output generated by it when fed by a specific phase sequence is shown in Fig. 6. The computational complexity of the TPU algorithm is extremely small, since it requires only 9 *floating point operations* (FLOPS) for each frame..[7] Unluckily, the TPU algorithm fails in the presence of phase variations exceeding π. In principle, the amplitude of such variations can be reduced by making the time interval between two subsequent phase measurements shorter (i.e., T_F smaller). In fact, this increases the value of the maximum target speed

$$v_c = \frac{\lambda}{4T_F}, \tag{15}$$

that allows an unambiguous phase unwrapping. In fact, the TPU algorithm works if the target speed belongs to the interval.[8] $[-v_c, v_c)$ or, equivalently, if the rate of phase variations does not exceed

$$\omega_c = \frac{\pi}{T_F}. \tag{16}$$

Unluckily, T_F cannot be arbitrarily reduced because of hardware limitations. This motivates the development of new phase unwrapping algorithms that are able to work properly at target speeds greater than v_c (15).

Algorithm 1 Example of traditional phase unwrap implementation

Input: $\{\phi_k\}$
Initialize:
$\psi_1 = \phi_1$
Begin:
for $k = 2$ to $k = N_F$ **do**
  $\beta_k = \lfloor \lfloor (\psi_{k-1} - \phi_k)/\pi \rfloor /2 + 0.5 \rfloor$
  $\psi_k = \phi_k + 2\pi\beta_k$
end for
Output: $\{\psi_k\}$

4. Doppler-based phase unwrapping algorithm

In this section, a novel algorithm for performing phase unwrapping, called *Doppler-assisted phase unwrapping* (DAPU), is illustrated. It exploits the Doppler information acquired from multiple chirps of the same frame to make accurate phase unwrapping possible in those cases in which, because of the low frame rate and/or high target speed, TPU fails. In the following, its description is provided for the case in which $N_c = 2$ (i.e., two chirps are transmitted in each frame; see Fig. 2), for simplicity. The DAPU algorithm is fed by the sequence of couples of wrapped phases $\{(\phi_{1,k}, \phi_{2,k}); k = 1, 2, \dots\}$. The first phase of each couple (namely, $\phi_{1,k}$) is evaluated in the same way as the phase processed by TPU algorithm. Therefore, it represents the phase of a specific element of the matrix $\mathbf{S}_\mathrm{A}$ evaluated for the first chirp of the kth frame (this matrix is denoted $\mathbf{S}_\mathrm{A}^{(1)}[k]$); the row and column index of this element, denoted $\bar{l}_k^{(1)}$ and $\bar{m}_k^{(1)}$, respectively, are evaluated by searching for an amplitude peak in the set of elements of the matrix $\mathbf{S}_\mathrm{A}^{(1)}[k]$. On the other hand, the phase $\phi_{2,k}$ represents the phase of the element $(\bar{l}_k^{(1)}, \bar{m}_k^{(1)})$ of the matrix $\mathbf{S}_\mathrm{A}$ evaluated for the second chirp of the kth frame (this matrix is denoted $\mathbf{S}_\mathrm{A}^{(2)}[k]$). For this reason, for any k, the phases of the couple $(\phi_{1,k}, \phi_{2,k})$ refer to two consecutive chirps of the same (i.e., the kth) frame, but are associated with measurements referring to the same spatial coordinates (i.e., to the same range and azimuth). Based on the sequence $\{(\phi_{1,k}, \phi_{2,k}); k = 1, 2, \dots\}$, the DAPU algorithm computes:

[7] A detailed analysis of the TPU computational cost is illustrated in Appendix A
[8] This interval is called *Doppler unambiguity region*

(1) The phase sequence $\{(\alpha_{1,k}, \alpha_{2,k}); k = 1, 2, \ldots\}$ (with $\alpha_{1,1} = \phi_{1,1}$) resulting from TPU of $\{(\phi_{1,k}, \phi_{2,k}); k = 1, 2, \ldots\}$;
(2) The phase sequence $\{\psi_k; k = 1, 2, \ldots\}$ (with $\psi_1 = \phi_{1,1}$), resulting from TPU of $\{\phi_{1,k}; k = 1, 2, \ldots\}$;
(3) The sequence $\{\bar{\omega}_k; k = 1, 2, \ldots\}$, where

$$\bar{\omega}_k \triangleq \frac{\alpha_{2,k} - \alpha_{1,k}}{T_C} \tag{17}$$

represents an estimate of rate of change of phase evaluated over the two consecutive chirps of the kth frame. Note that this estimate refers to the time instant

$$t_k^{(\bar{\omega})} \triangleq kT_F + \frac{T_C}{2} \tag{18}$$

that corresponds to the center of the time interval which the phases $\{\phi_{1,k}, \phi_{2,k}\}$ refer to; moreover, this instant can be approximated as kT_F, since $T_F \gg T_C$.

The DAPU algorithm operates in a recursive fashion. The processing it executes for the kth frame interval aims at generating an estimate, denoted $\hat{\phi}_k^{(u)}$, of the unwrapped phase referring to that interval. The evaluation of $\hat{\phi}_k^{(u)}$ is based on

(a) the estimates $\{\bar{\omega}_k, \bar{\omega}_{k+1}, \bar{\omega}_{k+2}\}$ of the rate of change of phase in the considered frame interval and in the following two frame intervals;
(b) the previous estimate $\hat{\phi}_{k-1}^{(u)}$ of the unwrapped phase
(c) the estimates $\{\hat{\omega}_{k-1}, \hat{\omega}_{k-2}, \hat{\omega}_{k-3}\}$ of the rate of the past change of phase, evaluated on the basis of the *unwrapped* phase; in fact, $\hat{\omega}_{k-l}$, being defined as

$$\hat{\omega}_{k-l} \triangleq \frac{\hat{\phi}_{k-l}^{(u)} - \hat{\phi}_{(k-l)-1}^{(u)}}{T_F}, \tag{19}$$

can be considered as an estimate *average* rate of phase variation over the time interval $((k-1-l)T_F, (k-l)T_F)$, centered at the instant

$$t_k^{(\hat{\omega})} \triangleq T_F \frac{(k-1-l) + (k-l)}{2}, \tag{20}$$

with $l \in \{1, 2, 3\}$.

The DAPU algorithm tries to compute a more accurate estimate of the average rate of change of phase in the time interval $((k-1)T_F, kT_F)$ by fitting its trend over a larger observation interval with a polynomial and, in particular, with a quadratic function. In practice, we take into consideration the vector of measurements

$$\mathbf{\Omega}^{(k)} \triangleq \left[\hat{\omega}_{k-3}, \hat{\omega}_{k-2}, \hat{\omega}_{k-1}, \bar{\omega}_k, \bar{\omega}_{k+1}, \bar{\omega}_{k+2}\right]^{\mathrm{T}} \tag{21}$$

and the vector of the associated abscissas

$$\mathbf{x} \triangleq [-3.5, -2.5, -1.5, 0, 1, 2]^{\mathrm{T}} \tag{22}$$

that represent the corresponding normalized instants at which such measurements refer to; note that, in the evaluation of each abscissa, normalization is accomplished with respect to the frame interval T_F and that the instant kT_F is taken a reference. Therefore, if we adopt the model $y = ax^2 + bx + c$ to fit the available measurements, the least-square estimate of the coefficients $\hat{a}^{(k)}$, $\hat{b}^{(k)}$ and $\hat{c}^{(k)}$ can be expressed as (e.g., see [33])

$$[\hat{a}^{(k)}, \hat{b}^{(k)}, \hat{c}^{(k)}]^{\mathrm{T}} = (\mathbf{X}^{\mathrm{T}}\mathbf{X})^{-1}\mathbf{X}^{\mathrm{T}}\mathbf{\Omega}^{(k)}, \tag{23}$$

where

$$\mathbf{X} \triangleq \left[\mathbf{x}^{(2)}, \mathbf{x}, [1, 1, 1, 1, 1, 1]^{\mathrm{T}}\right], \tag{24}$$

and $\mathbf{x}^{(2)}$ represents the vector obtained from $\mathbf{x}$ by replacing each element with its square. Then, the average rate of change of phase in the time interval $((k-1)T_F, kT_F)$ is evaluated as

$$\hat{\omega}_k^{(a)} = \hat{a}^{(k)}x^2 + \hat{b}^{(k)}x + \hat{c}^{(k)}\Big|_{x=-0.5}. \tag{25}$$

Note that the choice of evaluating the quadratic function for $x = -0.5$ (i.e., at the instant $(k-0.5)T_F$) is motivated by the fact that the rate of phase change is assumed to vary in a linear fashion during any interval lasting T_F.

Given $\hat{\omega}_k^{(a)}$ (25), an estimate $\hat{\gamma}^{(k)}$ of the overall number of complete phase rotations around the origin $\gamma^{(k)}$ between the $(k-1)$th frame and the kth frame is evaluated as

$$\hat{\gamma}^{(k)} = \left\lfloor \frac{\hat{\omega}_k^{(a)}T_F - (\psi_k - \psi_{k-1})}{2\pi} \right\rceil, \tag{26}$$

where $\lfloor\cdot\rceil$ represents the *nearest integer* rounding function. Given $\hat{\gamma}^{(k)}$ (26), the new unwrapped phase $\hat{\phi}_k^{(u)}$ is computed as

$$\hat{\phi}_k^{(u)} = \hat{\phi}_{k-1}^{(u)} + \psi_k - \psi_{k-1} + 2\pi\hat{\gamma}^{(k)}, \tag{27}$$

since the difference $(\psi_k - \psi_{k-1})$ accounts for the phase variation from the $(k-1)$th frame to the kth one in the absence of complete phase rotations. This concludes our description of the DAPU algorithm.

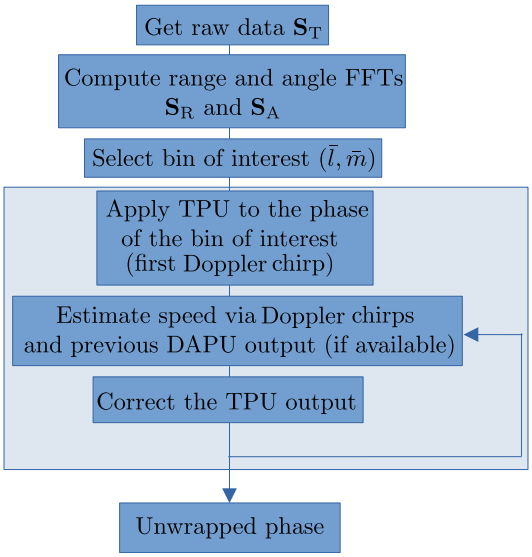

Fig. 7. Representation of the basic steps involved in the DAPU algorithm.

It is important to point out that:

(1) The DAPU algorithm can be initialized by setting: a) $\hat{\phi}_{-3}^{(u)} = \hat{\phi}_{-2}^{(u)} = \hat{\phi}_{-1}^{(u)} = \hat{\phi}_{0}^{(u)} = 0$ when $\hat{\omega}_1^{(a)}, \dots, \hat{\omega}_3^{(a)}$ are evaluated; b) $\psi_0 = \psi_1$ when $\hat{\gamma}^{(1)}$ and $\hat{\phi}_1^{(u)}$ are computed.

(2) If T_F is reasonably small, the trajectory described by the six measurements collected in $\mathbf{\Omega}^{(k)}$(21) is expected to be well represented by a parabolic trajectory.

(3) The first three elements of $\mathbf{\Omega}^{(k)}$ (21) have the purpose of giving stability and memory to the estimation, whereas its last three elements have the role of changing the trend of the curve.

(4) For any k, the phases $\phi_{1,k}$ and $\phi_{2,k}$ can be quickly acquired within the kth frame, whereas a much longer time is required to acquire these information from the next frame, as evidenced by Fig. 2. 5) The target maximum speed at which the DAPU algorithm can operate is (see Eq. (17))

$$v_c^{(\mathrm{DAPU})} = \frac{\lambda}{4T_C}, \tag{28}$$

and is much higher than the maximum unambiguous speed of the TPU algorithm (see (15)).

The DAPU algorithm is summarized in Algorithm 2. A simple block diagram representing its flow is shown in Fig. 7. The DAPU computational cost is assessed in Appendix A.

The recursive nature and initialization of the DAPU algorithm play a crucial role in ensuring its proper functioning. The initialization process for both the TPU and DAPU algorithms begins with selecting an appropriate range-angle bin from the 2D FFT output. This selection should be guided by the engineers understanding of the environment. A simple approach, in the case of a single target in front of the radar, is to choose the bin with the highest amplitude and analyze its phase evolution over time. However, in Algorithm 2, all parameters are set to zero by default. This assumption implies that the target remains stationary during the first six acquired frames. If the target is moving, a phase unwrapping error initially occurs. However, after these six frames, the algorithm converges and begins correctly tracking the target. Finally, it is worth noting that the algorithm can accommodate different radar configurations or a different number of virtual arrays. Increasing the number of virtual antennas improves the SNR by reducing the size of each range-angle bin. However, the DAPU unwrapping algorithm is completely agnostic to the number of antennas used by the radar.

5. Experimental results

In this section the improvement provided by the DAPU algorithm with respect to the TPU algorithm is assessed in the estimation of small displacements. In the following, we first describe the radar device employed in our measurement campaigns. Then, we analyze various numerical results obtained on the basis of the measurements acquired in two different scenarios, namely in a structure testing laboratory and on a steel footbridge. The experiment accomplished in the laboratory enabled the validation of the DAPU algorithm under controlled conditions, while the experiments conducted on the steel footbridge allowed us to assess its applicability to real-world scenarios.

Algorithm 2 Doppler-assisted phase unwrap algorithm.

Input: $\{(\phi_{1,k}, \phi_{2,k})\}$.
Initialize:
$\hat{\phi}^{(u)}_{-3}, ..., \hat{\phi}^{(u)}_{0} = 0$.
$\mathbf{x} = [-3.5, -2.5, -1.5, 0, 1, 2]^{\mathrm{T}}$.
$\mathbf{X} \triangleq \left[\mathbf{x}^{(2)}, \mathbf{x}, [1, 1, 1, 1, 1, 1]^{\mathrm{T}}\right]$.
$\{\psi_k\}$ as TPU of $\{\phi_{1,k}\}$.
$\psi_0 = \psi_1$.
Begin:
for $k = 1, 2, ...$ **do**
  $(\alpha_{1,k}, \alpha_{2,k})$ as TPU of $(\phi_{1,k}, \phi_{2,k})$.
  $\bar{\omega}_k \triangleq \frac{\alpha_{2,k} - \alpha_{1,k}}{T_C}$ (see (17)).
  $\hat{\omega}_{k-l} \triangleq \frac{\hat{\phi}^{(u)}_{k-l} - \hat{\phi}^{(u)}_{(k-l)-1}}{T_F}, l = 1, 2, 3$ (see (19)).
  $\mathbf{\Omega}^{(k)} \triangleq \left[\hat{\omega}_{k-3}, \hat{\omega}_{k-2}, \hat{\omega}_{k-1}, \bar{\omega}_k, \bar{\omega}_{k+1}, \bar{\omega}_{k+2}\right]^{\mathrm{T}}$ (see (21)).
  $[\hat{a}^{(k)}, \hat{b}^{(k)}, \hat{c}^{(k)}]^{\mathrm{T}} = (\mathbf{X}^{\mathrm{T}}\mathbf{X})^{-1}\mathbf{X}^{\mathrm{T}}\mathbf{\Omega}^{(k)}$ (see (23)).
  $\hat{\omega}^{(a)}_k = \hat{a}^{(k)}x^2 + \hat{b}^{(k)}x + \hat{c}^{(k)}\Big|_{x=-0.5}$ (see (25)).
  $\hat{\gamma}^{(k)} = \lfloor [\rceil \frac{\hat{\omega}^{(a)}_k T_F - (\psi_k - \psi_{k-1})}{2\pi}$ (see (26)).
  $\hat{\phi}^{(u)}_k = \hat{\phi}^{(u)}_{k-1} + \psi_k - \psi_{k-1} + 2\pi\hat{\gamma}^{(k)}$ (see (27)).
end for
Output: $\{\hat{\phi}^{(u)}_k, k = 1, 2, ...\}$.

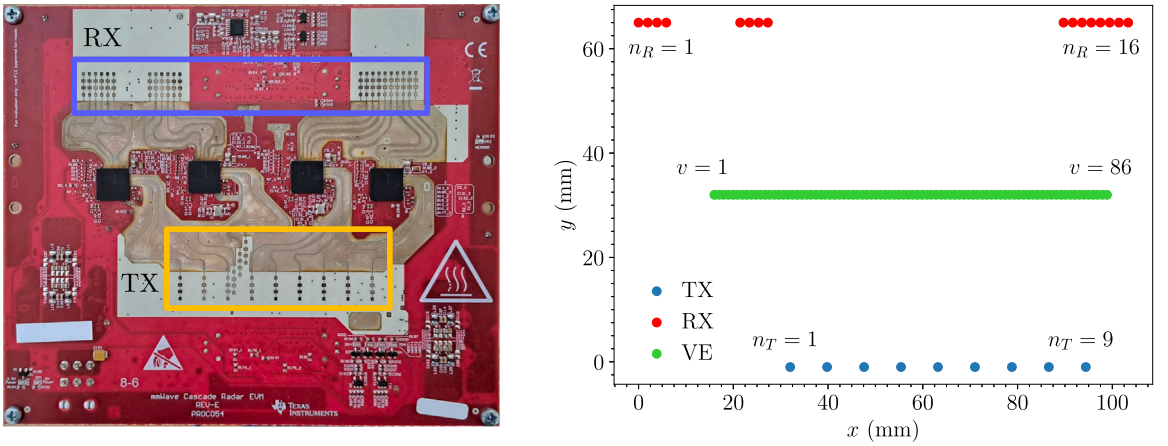

(a) (b)

Fig. 8. (a) Employed MIMO radar device and (b) representation of the physical TX and RX arrays (the employed virtual ULA is also shown); n_R represents the RX antenna index.

5.1. MIMO radar device

All the measurements have been acquired through a FMCW TIDEP-01012 Cascade mmWave radar evaluation module, which is designed and manufactured by Texas Instruments Inc. and is readily available as an off-the-shelf device [34]. This device is endowed with a planar array made of 12 TX and 16 RX antennas, so that the total number of available VAs is 192; however, only 9 TX antennas are used in our work, since a uniform linear portion of the whole virtual array is exploited; in practice, after virtual array reordering, only 86 virtual elements are used with an interantenna spacing is equal to $\lambda/4$. The relevant parameters adopted in our experiments are: a) chirp slope $\mu = 87$ MHz/μs; b) central frequency $f_c = 78$ GHz (corresponding to the wavelength $\lambda = 3.75$ mm); c) sampling frequency $f_s = 10$ MHz; d) number of samples per chirp $N = 512$; e) chirp duration $T_C = 64$ μs; f) frame duration $T_F = 30$ *ms*. Moreover, range and angle FFTs of order $N_0^{(\mathrm{R})} = 1024$ and $N_0^{(\mathrm{A})} = 128$, respectively, have been used. A picture of the employed radar device and a representation of the physical TX and RX arrays, together with the employed virtual ULA, are provided in Figs. 8-(a) and -(b), respectively.

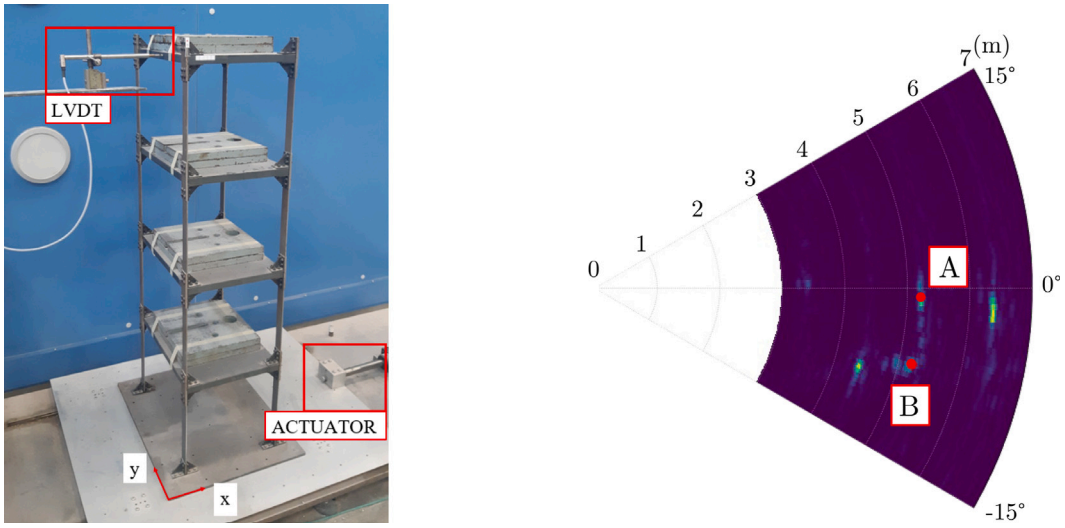

(a) (b)

Fig. 9. Laboratory experiments: (a) picture of the steel frame employed in our measurement campaign; (b) polar representation of a portion of the matrix $\mathbf{S}_A$ acquired in front of the considered frame (the position of the two points selected for phase estimation is identified by red circles).

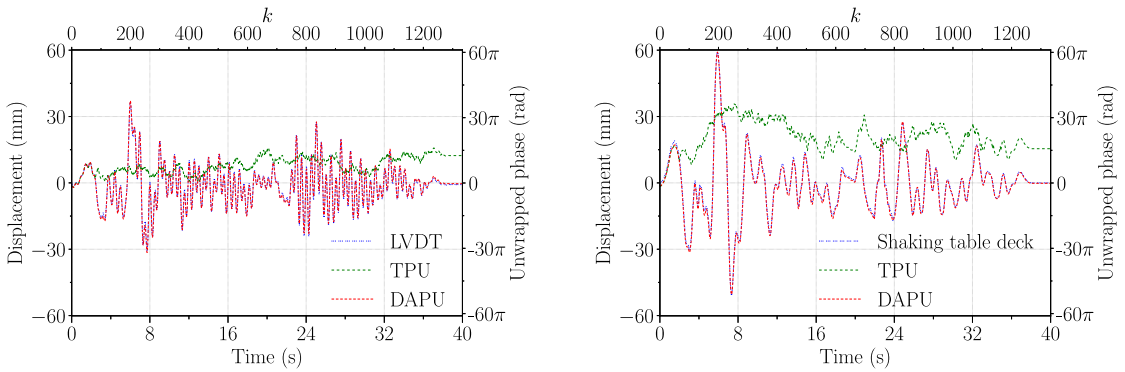

(a) (b)

Fig. 10. Temporal evolution of the displacements characterizing: (a) point A; (b) point B. The measurements provided by the reference sensor are compared with the estimates generated by the TPU and DAPU algorithms.

5.2. Laboratory experiments

These experiments have been performed under controlled conditions, and have involved the four-story steel frame shown in Fig. 9-(a); this frame has been put on a shaking table exciting it. Different types of excitation were applied to the frame base; these included sinusoidal forces and simulated earthquake ground motions. Our radar system was used to estimate the displacements of multiple points of the frame in all the experiments; such points were characterized by different heights. The accuracy of radar-based estimates has been assessed by comparing them with the estimates provided by a reference sensor, namely a LVDT sensor. The last sensor is able to assess displacements with the range [0, 100 mm]; moreover, its sensitivity and excitation voltage are equal to 80 mV/V and 10 V, respectively.

Our first results refer to the displacements due to a simulated earthquake ground motion, lasting 38 s and featuring fast displacements with a maximum amplitude of 60 mm; this condition presented the most significant challenges for the phase unwrapping process because of the presence of wide and fast movements. With the given radar settings, the spectral peak associated with the main reflection may move from one range bin to another one (i.e., in principle, the value of $\bar{l}$ is not constant). In this case, we can rely on the leakage of the reflected power over multiple adjacent bins at the expense of a degraded SNR, or employ a tracking algorithm to adjust $\bar{l}$ dynamically and compensate for the additional phase modulation that such approach can introduce. However, all this is outside the scope of this manuscript. A polar representation of the amplitude of the elements of the matrix $\mathbf{S}_A$ evaluated in one of our experiments is shown in Fig. 9-(b), where the position of the couple of points (one located at the bottom

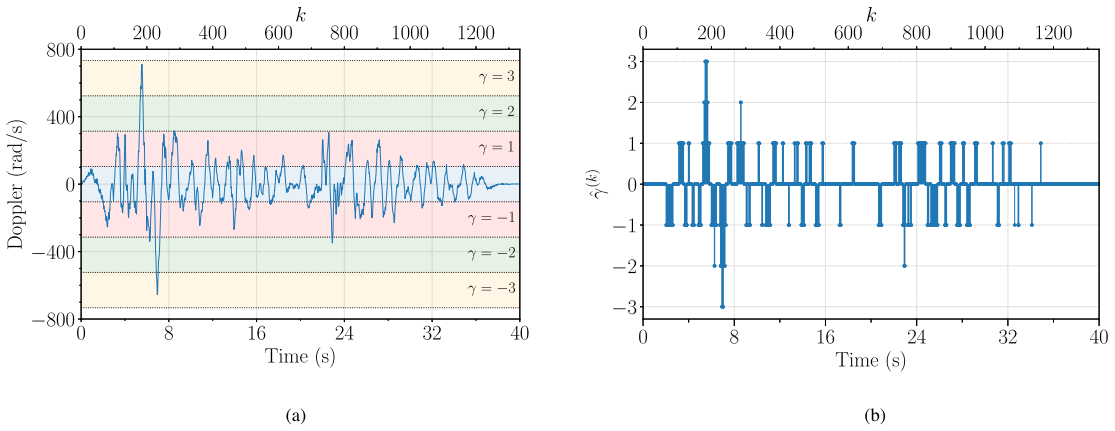

Fig. 11. Representation of: (a) the time evolution of Doppler rate; (b) the corresponding sequence of estimates $\{\hat{\gamma}^{(k)}\}$ generated by the DAPU algorithm (see (26)). All these results refer to point B (see Fig. 9-(b)).

of the frame and the other at its top) whose displacements are analyzed in the following are highlighted. These specific points (namely, point B located on the shaking table deck and point A located at the top of the frame) have been selected because they enabled a simple comparison with the available reference displacements; in fact, the displacement of point B was equal to that of shaking table deck, whereas that of point A was measured by a LVDT sensor. The reference displacements and the corresponding radar-based estimates obtained through the TPU and DAPU algorithms are shown in Fig. 10. The Doppler rate of point B, measured at the instants kT_F, is shown in Fig. 11(a); in that figure, seven colored stripes have been drawn to identify the Doppler rate intervals $\{[(2\gamma-1),(2\gamma+1)]\omega_c;\gamma=-3,\dots,3\}$. The corresponding values of the parameter $\hat{\gamma}$ generated by the DAPU algorithm (see (26)) are shown in Fig. 11(b). A detailed representation of the instantaneous displacement of point B, its Doppler rate and the corresponding values of $\hat{\gamma}$ generated by the DAPU algorithm is offered in Fig. 12.

From these results it is easily inferred that:

(1) The TPU algorithm operates in a reliable fashion only when the frame oscillations are small and slow: as soon as the displacement occurring between two frames exceeds $\lambda/4 \approx 0.94$ mm (i.e., the rate of phase variation observed for the considered point is greater than $\omega_c \approx 104$ rad/s), it fails (see Fig. 12-(a)).

(2) The DAPU algorithm, instead, is able to track rapid displacements and to generate accurate estimates of them (see Fig. 12-(a)). This is made possible by its ability to filter noisy Doppler information and to properly assess the overall number of phase rotations due to Doppler (see Figs. 12-(b) and 12-(c)).

(3) The non-zero estimates of γ do not precisely align with the time instants at which the phase rotation rate exceeds ω_c (16) (see Figs. 12-(b) and 12-(c)). Note that, if $\hat{\gamma}$ had been evaluated on the basis of unfiltered Doppler measurements, the output of DAPU shown Fig. 12-(a) would not have followed the reference signal; instead, it would have been affected by jumps similar to those observed at the output of the TPU algorithm.

5.3. Real footbridge experiments

The accuracy achieved by the TPU and DAPU algorithms has been also assessed by measuring the displacements experienced by a slender and lightweight truss-girder steel footbridge spanning the Panaro River in Modena, Italy (see Fig. 13(a)). The considered footbridge is highly deformable and sensitive to dynamic vibrations, typically caused by the movement of pedestrians, cyclists, and environmental factors (e.g., wind). It is characterized by a box-shaped cross-section measuring 3.00 x 3.20 meters and is made up of truss girders constructed from hollow tubular sections. In total, the footbridge stretches over 160 meters and is divided into three segments: two 45-meter side spans and a central span of 70 m.

The employed radar device has been positioned beneath the footbridge (see Fig. 13(b)). Its alignment with the right side of the deck has allowed us to detect the vertical vibrations of points spread along the footbridge span that are also aligned to that side. The polar representation of the matrix $\mathbf{S}_A$ obtained in these conditions is illustrated in Fig. 13-(c), where the positions of the two points analyzed in the following (and denoted A and B) are also identified. These points are vertically in line with the radar device on the right side of the deck, but differ in their height. In fact, point A is located on a transverse element of the underside of the deck, whereas point B is associated with an higher element (which is likely to be part of the parapet). An accelerometer-based monitoring system has been also installed on the footbridge for comparison purposes. The main components of the measurement system are a controller, a storage unit and bus-connected biaxial sensing units of *Micro-Electro-Mechanical System* (MEMS) type. The bus connection guarantees a high degree of reliability and prevention against electromagnetic interferences. Thanks to an accurate design of the employed device and local digital filtering techniques, these sensing units exhibit a noise level of about 0.3–0.5 mg (depending on the sampling frequency), where g indicates the gravity acceleration [35]. In our measurement campaign, the MEMS biaxial accelerometers were placed in seven cross-sections of the footbridge, namely at the midspan and at six additional positions,

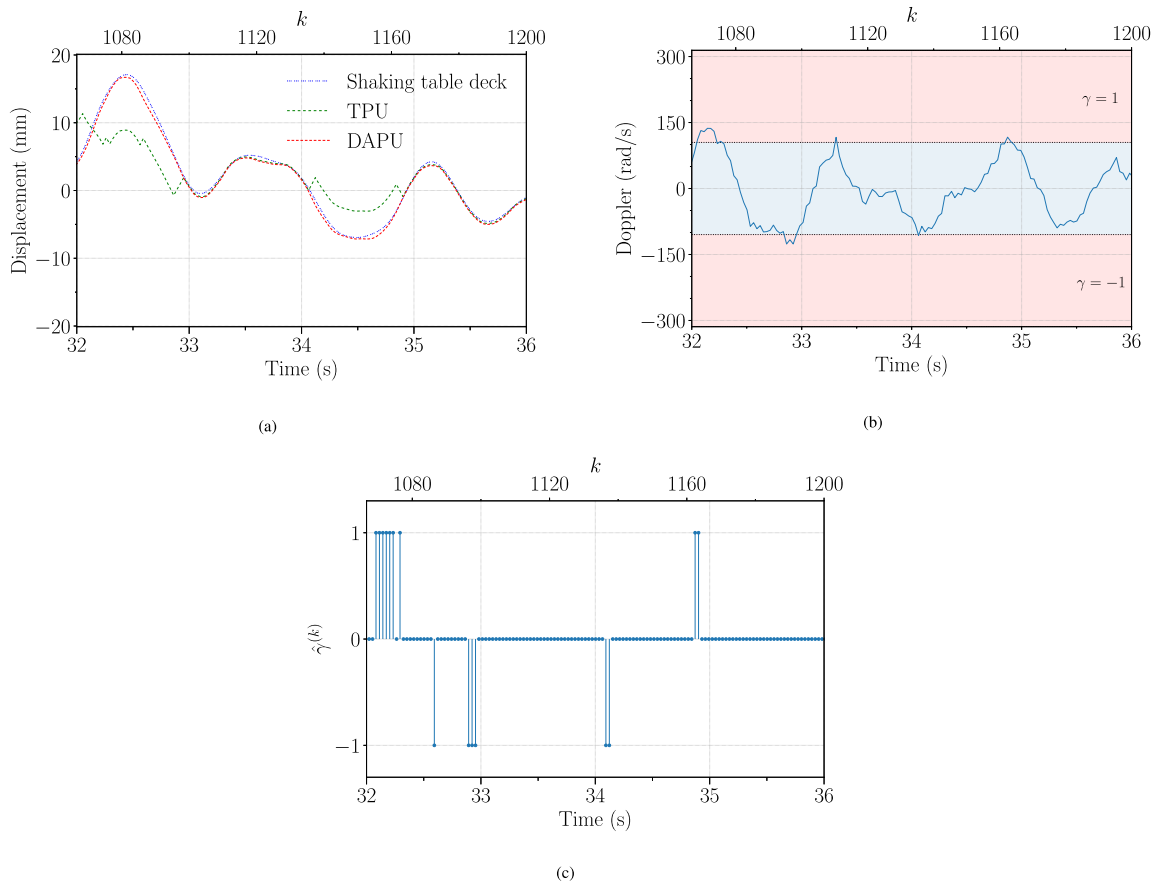

Fig. 12. Representation of: (a) the temporal evolution of the displacement of the controlled shaking table deck and of the corresponding estimates evaluated by the TPU and DAPU algorithms; (b) the Doppler rate estimated through our radar system; (c) the sequence of estimates $\{\hat{\gamma}^{(k)}\}$ generated by the DAPU algorithm (see (26)). All these results refer to point B (see Fig. 9-(b)). Note that the radar displacement estimated by the TPU and DAPU algorithms have been aligned with the table deck displacement for comparison purposes in subfigure (a).

symmetrically arranged around the midspan at intervals of 7.5 meters each. The accelerometers were installed on both sides of the footbridge deck using plates and magnets. The sampling frequency of the sensing system was set to 80 Hz.

Both acquisition systems measured structural vibrations due to environmental conditions and those induced by a pedestrian walking on the footobridge. The forced vibrations were generated by a pedestrian jumping at a frequency of 138 *beats per minute* (BPM). This specific frequency, controlled through a metronome, has been selected to excite the main vertical vibrational mode of the footbridge. The structural displacements estimated on the basis of our radar measurements, using the TPU and DAPU algorithms, have been compared with those estimated on the basis of the measured accelerations. The procedure outlined in [36] has been exploited to reconstruct displacements from measured accelerations; this requires minimizing the squared errors between the measured accelerations and the second-order time derivative of the reconstructed displacements. The choice of this algorithm was motivated by the fact that it produces accurate results when the overall temporal history of the observed displacement has zero mean.

The estimates of the structural displacements obtained from the measured accelerations are compared with those extracted from radar measurements in Fig. 14; in the same figure, the sequence of estimates $\{\hat{\gamma}^{(k)}\}$ generated by the DAPU algorithm for point A and the temporal evolution of the Doppler rate referring to the same point are also shown. Similar results are shown for point B in Fig. 15. Detailed views are shown in Figs. 16 and 17 for points A and B, respectively. These results evidence that:

(1) The DAPU algorithm is able to accurately track both small and large displacements, even under conditions of strong noise as those characterizing point B (see Figs. 15 and 16).

(2) In both cases there is a good agreement between the displacement derived from the measured acceleration and that estimated by the DAPU algorithm on the basis of the radar measurements. In particular, the maximum difference between these two displacements is approximately equal to 0.57 mm (the average of the absolute value of this difference is approximately equal to 0.17 mm). This confirms the effectiveness of the DAPU algorithm in successfully filtering out noisy Doppler samples and selecting the correct value of $\hat{\gamma}$.

(3) The use of the TPU algorithm leads to considerable inaccuracies in the estimated displacements (see Figs. 14-(a) and 15-(a)).

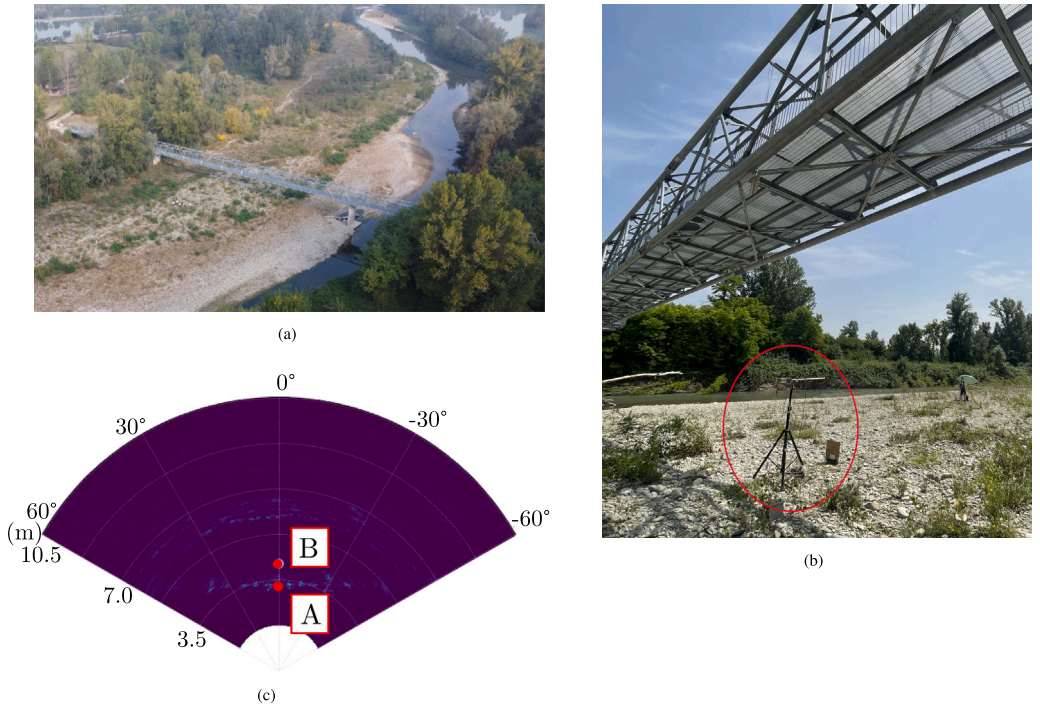

Fig. 13. Representation of the: (a) global view of the footbridge involved in our experiments; (b) the position of the employed radar device; (c) polar representation of the amplitude of the elements of the matrix $\mathbf{S}_A$ computed in one of our experiments. The position of the two points selected for displacement estimation is identified by red circles.

Finally, it is important to point out that, in this application, accurate estimates of displacements have been obtained through double integration of measured accelerations thanks to the fact that the considered footbridge oscillates around a position of zero displacement. In the presence of permanent or quasi-static displacements, this method could lead to considerable errors. On the contrary, radar-based estimates do not suffer from this problem and are unbiased in all conditions.

6. Conclusions

In this manuscript, a novel iterative method for mitigating the phase wrapping phenomenon in radar-based estimation of target displacement has been proposed. The accuracy of this method has been assessed by applying it to the estimation of dynamic structural displacements through a mmWave MIMO FMCW radar. Our results, based on a set of measurements acquired through a commercial radar device in two different scenarios, evidence that our method is able to carefully estimate the radial displacement of quickly moving structures, also in those situations where traditional solution fails, at the price of a small computational complexity.

CRediT authorship contribution statement

Giorgio Guerzoni: Writing – review & editing, Writing – original draft, Validation, Software, Methodology, Data curation, Conceptualization. **Elahe Faghand:** Writing – review & editing, Writing – original draft, Validation, Software, Methodology, Data curation, Conceptualization. **Loris Vincenzi:** Writing – review & editing, Writing – original draft, Validation, Supervision, Data curation, Conceptualization. **Elisa Bassoli:** Writing – review & editing, Writing – original draft, Validation, Data curation. **Giorgio Matteo Vitetta:** Writing – review & editing, Writing – original draft, Validation, Supervision, Methodology, Data curation, Conceptualization.

Declaration of competing interest

The authors declare that they have no known competing financial interests or personal relationships that could have appeared to influence the work reported in this paper.

Acknowledgments

This work was sponsored by the Department of Engineering ”Enzo Ferrari” of the University of Modena and Reggio Emilia via the research project “Radar MIMO per il monitoraggio della salute strutturale” in the scope of the research grant FARD2022. The financial support of the UNIMORE is gratefully acknowledged.

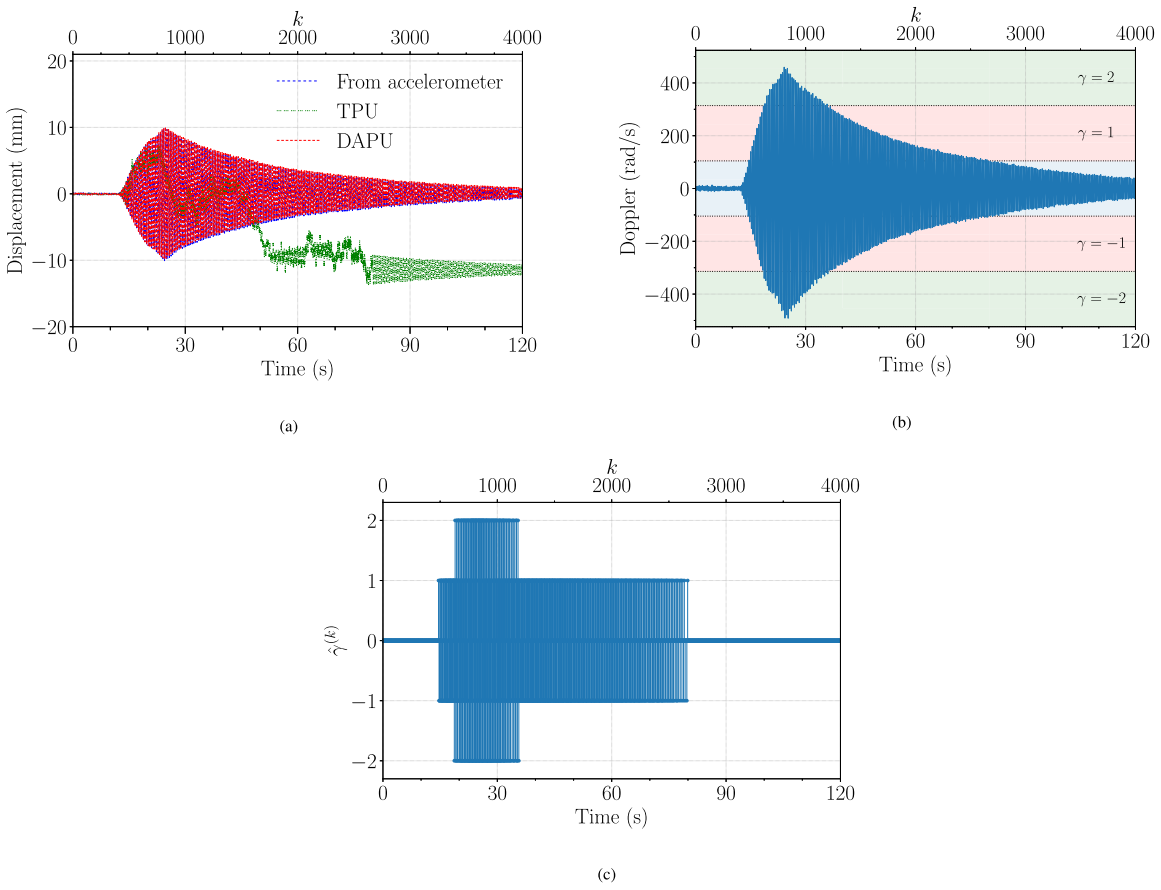

Fig. 14. Representation of the temporal evolution of: (a) the displacements estimated by the TPU algorithm, the DAPU algorithm and the accelerometer-based measurement system; (b) the estimated Doppler rate; (c) the corresponding sequence of estimates $\{\hat{\gamma}^{(k)}\}$ generated by the DAPU algorithm. All these results refer to point A.

Appendix A. Evaluation of TPU and DAPU computational complexity

In this Appendix, we assess the overall computational complexity of the TPU and DAPU methods in term of the number of FLOPS. In our evaluation, each summation, division, multiplication, and subtraction is counted as one flop. Based on the procedure illustrated in Algorithm 1, the computation of β_k and ψ_k requires 6 and 3 FLOPS, respectively. Therefore, for each new frame, the execution of the TPU algorithm requires 9 FLOPS. It is also worth mentioning that, in our simulations, performed on a AMD Ryzen 5 1400 at 3.2 GHz, the total time to unwrap 10000 samples is approximatively 0.03 s.

As far as the DAPU algorithm is concerned, its computational complexity is assessed as follows:

- Eq. (17) requires the evaluation of $(\alpha_{1,k}, \alpha_{2,k})$ using the TPU algorithm, with a cost of 18 FLOPS (9 FLOPS for each parameter) plus 2 FLOPS to evaluate $\bar{\omega}_k$.
- Eq. (19) requires 6 FLOPS in total.
- In Eq. (23) various matrix operations (namely, matrix multiplication and inversion) are performed; these involve the 6×3 matrix $\mathbf{X}$ and the 6 dimensional row vector $\mathbf{\Omega}$. These operations result in a total of 590 FLOPS.
- Finally, the computation of $\hat{\omega}_k^{(a)}$, $\hat{\gamma}^k$ and $\hat{\phi}_k^{(u)}$ according to Eqs. (25), (26) and (27) requires 4, 5 and 4 FLOPS, respectively.

Based on these results, it is easy to show that the overall number of FLOPS for the DAPU method is 620 (for each frame). This cost is still well within the capabilities of any modern personal computer. In our simulations, performed on a AMD Ryzen 5 1400 at 3.2 GHz, the total time to unwrap 10000 samples is approximatively 0.9 s; this results in a throughput exceeding 10000 samples per second.

Appendix B. Impact of noise on the TPU and DAPU algorithms

In this Appendix we briefly discuss how the presence of noise in radar measurements affects the accuracy of the TPU and DAPU algorithms in terms of probability of error.

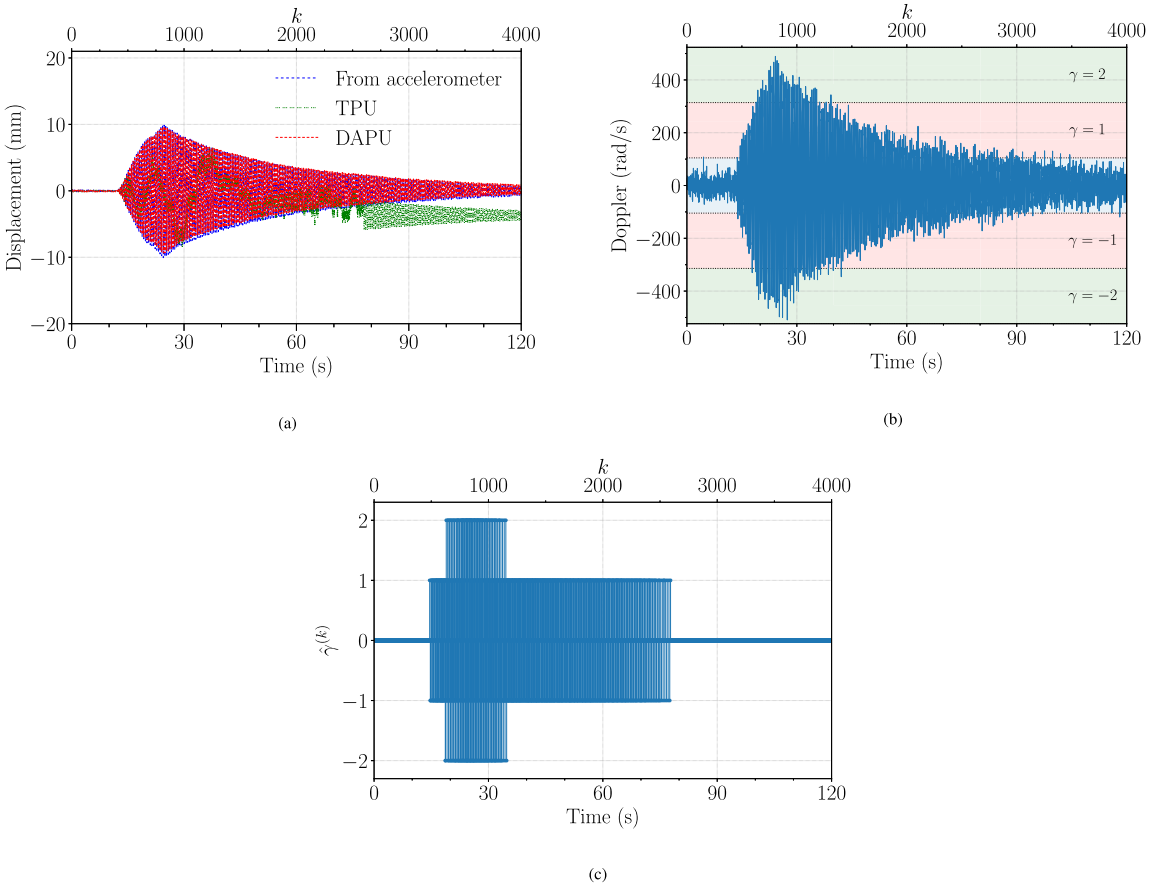

Fig. 15. Representation of the temporal evolution of: (a) the displacements estimated by the TPU algorithm, the DAPU algorithm and the accelerometer-based measurement system; (b) the estimated Doppler rate; (c) the corresponding sequence of estimates $\{\hat{\gamma}^{(k)}\}$ generated by the DAPU algorithm. All these results refer to point B.

B.1. TPU algorithm

The TPU algorithm is able to properly unwrap the phases if and only if the phase difference $\Delta\phi_k$ between two consecutive samples ϕ_k and ϕ_{k+1} is smaller than π; if a phase noise term η_k, drawn from a generic random distribution, is added to either ϕ_k or ϕ_{k+1}, then TPU will not fail if the condition

$$\Delta\phi_k + \eta_k < \pi \tag{29}$$

holds. Since the phase difference between two consecutive frames is proportional to the speed of the target (see Eq. (14)), phase trajectories associated with fast moving objects are more sensitive to noise. If we define v_k as the target speed at the instant kT_F, we can write the *probability of failure* of the TPU algorithm as a function of the target speed v_k, radar frame rate T_F and wavelength λ:

$$\mathbb{P}(e_{\text{TPU}}) = \mathbb{P}\left(\frac{4\pi}{\lambda} v_k T_F + \eta_k < \pi\right) \tag{30}$$

This expression is general, being independent of the specific distribution of η_k.

B.2. DAPU algorithm

Unlike TPU, a general expression for the probability of failure $\mathbb{P}(e_{\text{DAPU}})$ of the DAPU algorithm cannot be given. However, some useful insights are provided by an analysis of the internal structure of the algorithm itself. A key feature of the DAPU algorithm is represented by the fact that it computes the estimate $\hat{\omega}_k^{(a)}$ of the target speed (see Eq. (25)) and multiplies it by the frame duration T_F in order to assess the overall displacement experienced by the target between the kth and the $k-1$th frames; the estimation of $\hat{\omega}_k^{(a)}$ is based on $\bar{\omega}_k$, $\alpha_{1,k}$, $\alpha_{2,k}$, T_C and, in turn, on $\phi_{1,k}$ and $\phi_{2,k}$.

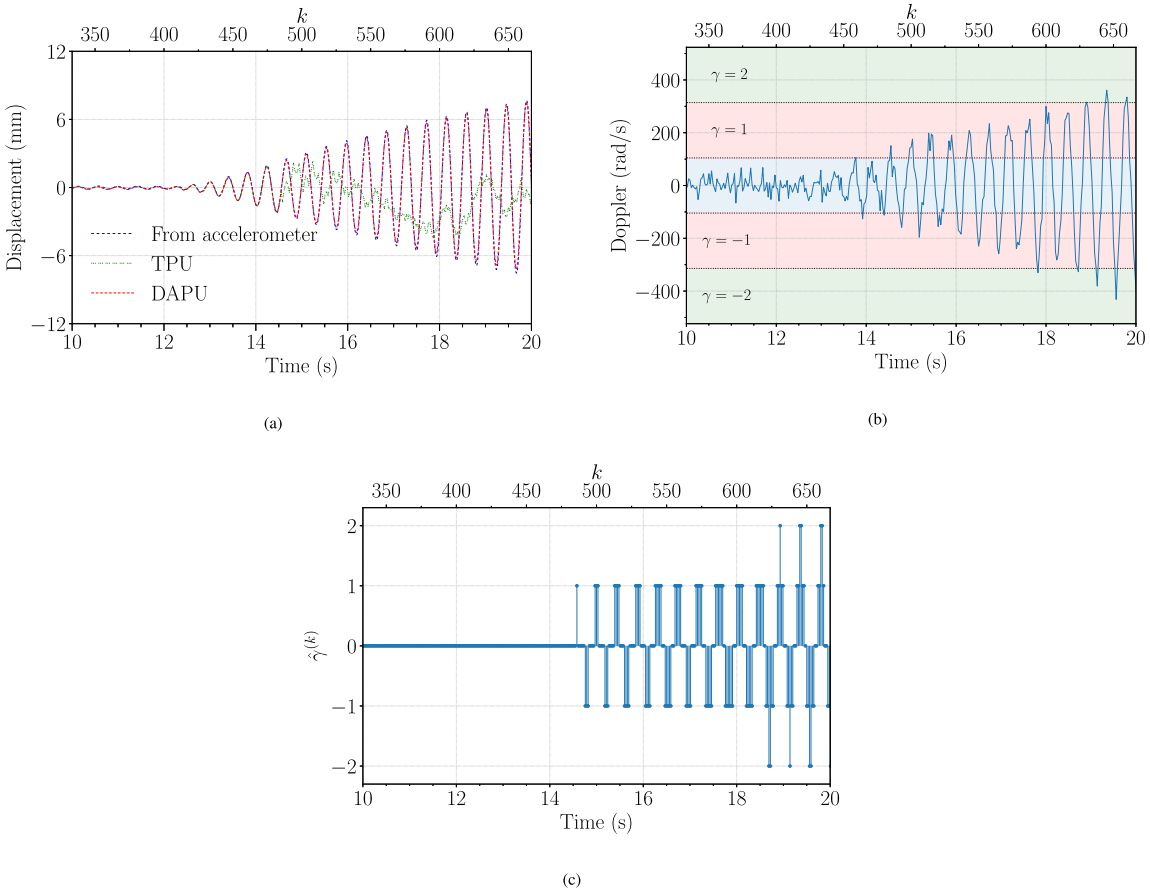

Fig. 16. Detailed representation of the temporal evolution of: (a) the displacements estimated by the TPU algorithm, the DAPU algorithm and the accelerometer-based measurement system; (b) the estimated Doppler rate; (c) the corresponding sequence of estimates $\{\hat{\gamma}^{(k)}\}$ generated by the DAPU algorithm. All these results refer to point B.

Let $\eta_{1,k}$ and $\eta_{2,k}$ denote the random noise samples superimposed to $\phi_{1,k}$ and $\phi_{2,k}$, respectively. The impact of $\eta_{1,k}$ and $\eta_{2,k}$ on the estimation of $\hat{\omega}_k^{(a)}$ becomes stronger if T_C is reduced. Moreover, an error in the estimation of $\eta_{1,k}$ will affect the estimation of the total inter-frame displacement more severely for larger values of T_F, but only if $\eta_{1,k}$ and $\eta_{2,k}$ are *uncorrelated*. If $\eta_{1,k}$ and $\eta_{2,k}$ are correlated, the estimation of $\hat{\omega}_k^{(a)}$ will be affected to a smaller extent. Based on the considerations illustrated above, it should be expected that

$$\mathbb{P}(e_{\mathrm{DAPU}}) \propto \frac{T_F}{T_C}, \rho_{1,2}^{-1} \tag{31}$$

where $\rho_{1,2}$ denotes the covariance between $\eta_{1,k}$ and $\eta_{2,k}$. Since $\phi_{1,k}$ and $\phi_{2,k}$ are separated by T_C seconds and $T_C \ll T_F$, $\rho_{1,2}$ is likely to be greater than zero in the considered scenarios.

B.3. Numerical results

Some computer simulations have been run to assess the TPU and DAPU probability of failure. The following assumptions have been made: 1) η_k, $\eta_{1,k}$ and $\eta_{2,k}$ are Gaussian random variables having zero mean and variances σ^2, σ_1^2 and σ_2^2, respectively; 2) $\eta_{1,k}$ and $\eta_{2,k}$ are correlated (their correlation coefficient is denoted $\rho_{1,2}$). In the case of the TPU algorithm, a noiseless phase trajectory $\{\phi_k, k = 1, \ldots, 10000\}$ has been generated and then the noise sequence $\{\eta_k\}$ has been added to it; the resulting sequence has been applied to the considered algorithm, whose probability of error has been evaluated as the ratio between the number of unwrapping errors and the length of the input sequence. A similar procedure has been followed for the DAPU algorithm, whose simulation has required, however, the generation of the sequences $\{\phi_{1,k}\}$ and $\{\phi_{2,k}\}$, and of the associated noise sequences$\{\eta_{1,k}\}$ and $\{\eta_{2,k}\}$, respectively. Our numerical results, referring to a (single) target moving at a constant speed, are illustrated in Figs. 18–20. In particular, the results shown in the first figure show the impact of noise variance on the failure probability of the TPU algorithm for three different target speeds; $T_F = 30$ ms and $T_C = 64$ μs, (resulting in $T_F/T_C = 468.75$) are assumed. Note that, as the target speed approaches the critical speed v_c, the TPU performance undergoes a significant degradation. The results shown in Fig. 19,

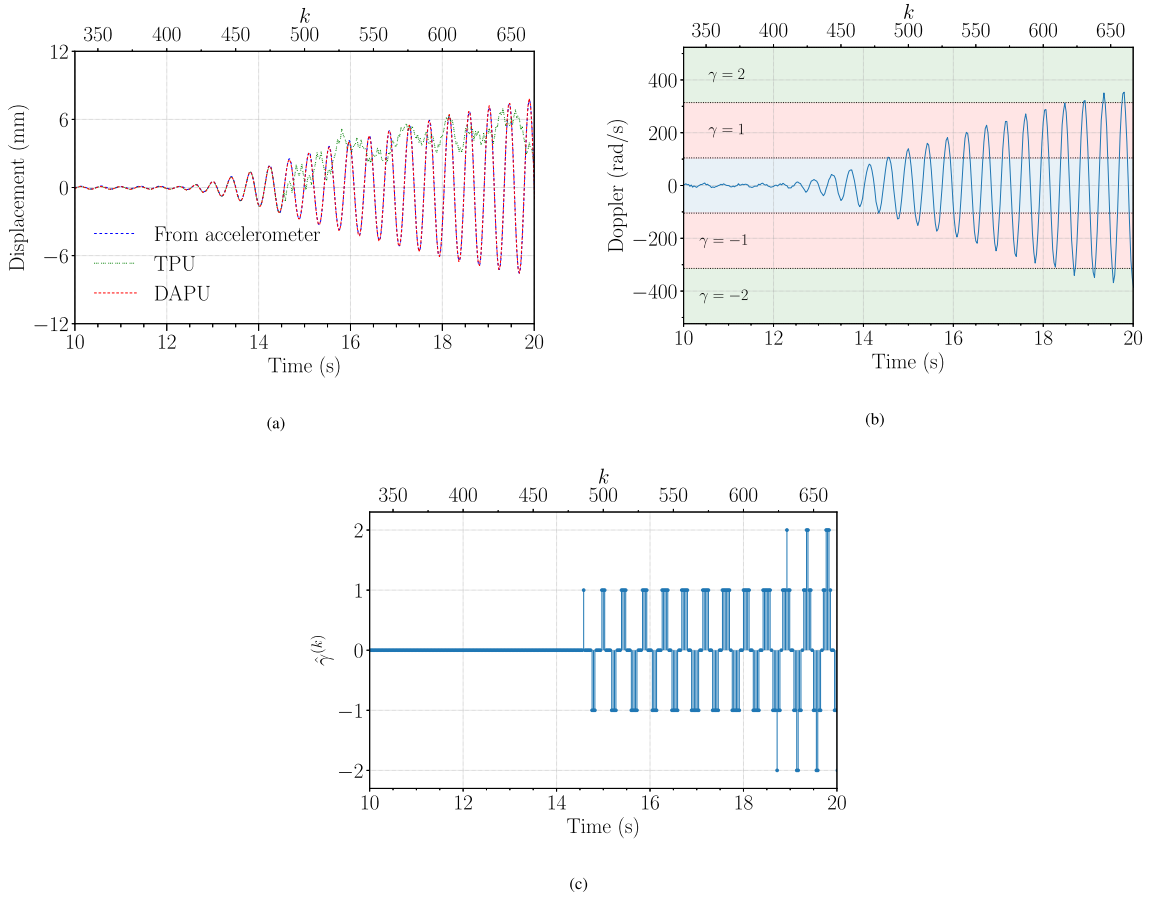

Fig. 17. Detailed representation of the temporal evolution of: (a) the displacements estimated by the TPU algorithm, the DAPU algorithm and the accelerometer-based measurement system; (b) the estimated Doppler rate; (c) corresponding sequence of estimates $\{\hat{\gamma}^{(k)}\}$ generated by the DAPU algorithm. All these results refer to point A.

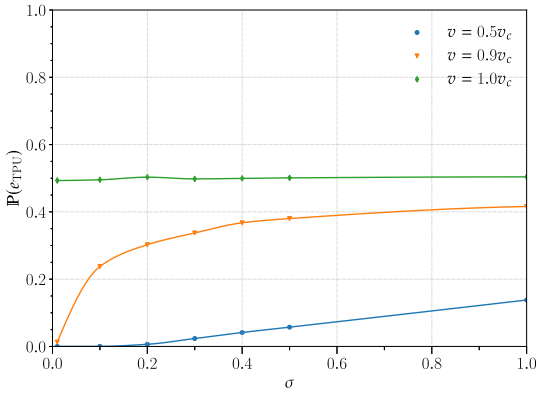

Fig. 18. TPU probability of failure vs noise variance for three different values of target speed.

instead, refer to the DAPU algorithm and aim at unveiling the impact of noise correlation on its probability of failure; in this case, three different values of the noise variances σ_1^2 and σ_2^2 are considered and $v = 30$ mm/s (corresponding to a Doppler rate of change $\omega \approx 400$ rad/s) is assumed for the target speed (the values of T_F and T_C are the same as the previous case). From these results it is easily inferred that, as noise correlation increases, the impact of noise on the DAPU algorithm becomes less significant; note that this is in agreement with Eq. (31). In Fig. 20, the dependence of the failure probability of the DAPU algorithm on the T_F/T_C ratio

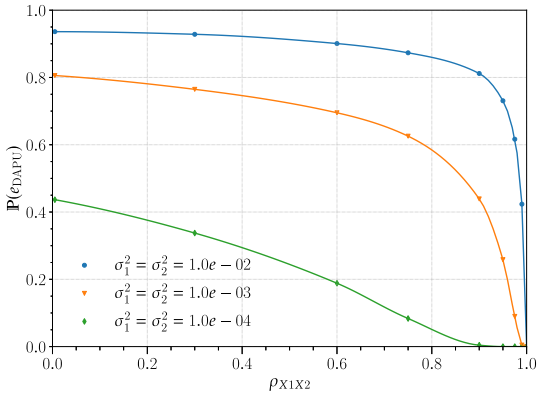

Fig. 19. DAPU probability of failure vs noise correlation for three different values of the noise variances σ_1^2 and σ_2^2.

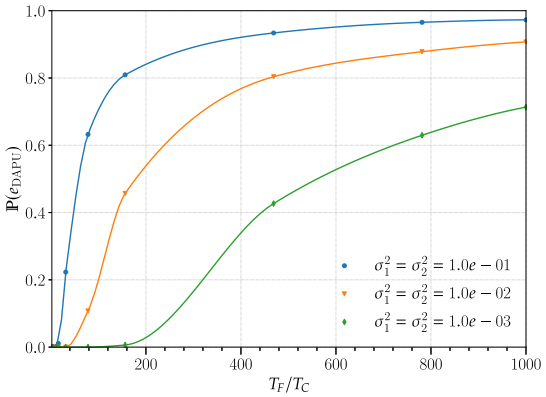

Fig. 20. DAPU probability of failure vs T_F/T_C ratio for three different values of the noise variances σ_1^2 and σ_2^2.

is shown; in this case, $T_F = 30$ ms, $\rho_{1,2} = 0.9$ and $v = 30$ mm/s are assumed and, similarly as in Fig. 19, three different values of the noise variances σ_1^2 and σ_2^2 are considered. These results lead to the conclusion that, as the ratio T_F/T_C increases, the probability of failure worsens, as suggested by Eq. (31).

Finally, it is worth noting that increasing the number of virtual antennas impacts the computational complexity primarily by increasing the complexity of the FFT angle, as a larger number of virtual antennas leads to a higher-dimensional FFT computation. However, the increased N_{VA} does not directly affect the computational complexity of the TPU or DAPU algorithms, as they process the phase sequence extracted from the 2D FFT independently of the number of antennas.

Data availability

Data will be made available on request.

References

[1] K. Kim, H. Sohn, Dynamic displacement estimation by fusing LDV and LiDAR measurements via smoothing based Kalman filtering, Mech. Syst. Signal Process. 82 (2017) 339–355.

[2] P.L. Reu, D.P. Rohe, L.D. Jacobs, Comparison of DIC and LDV for practical vibration and modal measurements, Mech. Syst. Signal Process. 86 (2017) 2–16.

[3] D. Lydon, M. Lydon, S. Taylor, J.M. Del Rincon, D. Hester, J. Brownjohn, Development and field testing of a vision-based displacement system using a low cost wireless action camera, Mech. Syst. Signal Process. 121 (2019) 343–358.

[4] B. Hosseiny, J. Amini, H. Aghababaei, Structural displacement monitoring using ground-based synthetic aperture radar, Int. J. Appl. Earth Observ. Geoinformat. 116 (2023) 103144.

[5] A. Ozdagli, B. Liu, F. Moreu, Low-cost, efficient wireless intelligent sensors (LEWIS) measuring real-time reference-free dynamic displacements, Mech. Syst. Signal Process. 107 (2018) 343–356.

[6] J.-W. Park, S.-H. Sim, H.-J. Jung, Displacement estimation using multimetric data fusion, IEEE/ASME Trans. Mechatronics 18 (6) (2013) 1675–1682.

[7] E. Bassoli, L. Vincenzi, F. Grassi, F. Mancini, A multi-temporal DInSAR-based method for the assessment of the 3D rigid motion of buildings and corresponding uncertainties, J. Build. Eng. 73 (2023) 106738.
[8] D. Camassa, N. Vaiana, A. Castellano, Modal testing of masonry constructions by ground-based radar interferometry for structural health monitoring: A mini review, Front. Built Environ. 8 (2023).
[9] C. Castagnetti, E. Bassoli, L. Vincenzi, F. Mancini, Dynamic assessment of masonry towers based on terrestrial radar interferometer and accelerometers, Sensors 19 (6) (2019).
[10] G. Luzi, M. Crosetto, E. Fernández, Radar interferometry for monitoring the vibration characteristics of buildings and civil structures: Recent case studies in Spain, Sensors 17 (4) (2017).
[11] R.E. Alva, L.G. Pujades, R. González-Drigo, G. Luzi, O. Caselles, L.A. Pinzón, Dynamic monitoring of a mid-rise building by real-aperture radar interferometer: Advantages and limitations, Remote. Sens. 12 (6) (2020).
[12] J. Wang, Y. Hua, C. Fan, X. Huang, Precise scatter estimation of complex bridges with portable MMW SAR, in: 2022 7th International Conference on Signal and Image Processing, ICSIP, 2022, pp. 147–151.
[13] A. Baumann-Ouyang, J.A. Butt, D. Salido-Monzú, A. Wieser, MIMO-SAR interferometric measurements for structural monitoring: Accuracy and limitations, Remote. Sens. 13 (21) (2021).
[14] L. Ding, M. Ali, S. Patole, A. Dabak, Vibration parameter estimation using FMCW radar, in: 2016 IEEE International Conference on Acoustics, Speech and Signal Processing, ICASSP, 2016, pp. 2224–2228.
[15] W. Tian, Y. Li, C. Hu, Y. Li, J. Wang, T. Zeng, Vibration measurement method for artificial structure based on MIMO imaging radar, IEEE Trans. Aerosp. Electron. Syst. 56 (1) (2020) 748–760.
[16] M. Pieraccini, F. Parrini, M. Fratini, C. Atzeni, P. Spinelli, M. Micheloni, Static and dynamic testing of bridges through microwave interferometry, NDT & E Int. 40 (3) (2007) 208–214.
[17] M. Pieraccini, L. Miccinesi, An interferometric MIMO radar for bridge monitoring, IEEE Geosci. Remote. Sens. Lett. 16 (9) (2019) 1383–1387.
[18] L. Miccinesi, M. Pieraccini, Bridge monitoring by a monostatic/bistatic interferometric radar able to retrieve the dynamic 3D displacement vector, IEEE Access 8 (2020) 210339–210346.
[19] Y. Xiong, Z. Peng, W. Jiang, Q. He, W. Zhang, G. Meng, An effective accuracy evaluation method for LFMCW radar displacement monitoring with phasor statistical analysis, IEEE Sensors J. 19 (24) (2019) 12224–12234.
[20] Y. Xiong, Z. Liu, S. Li, G. Meng, Z. Peng, Scanning microwave vibrometer: Full-field vibration measurement via microwave sensing with phase-encoded beam scanning, IEEE Trans. Instrum. Meas. 72 (2023) 1–11.
[21] Z. Ma, J. Choi, L. Yang, H. Sohn, Structural displacement estimation using accelerometer and fmcw millimeter wave radar, Mech. Syst. Signal Process. vol. 182 (2023) 109582.
[22] Q. Huang, S. Wei, L. Zhang, Radar interferometric phase ambiguity resolution using viterbi algorithm for high-precision space target positioning, IEEE Signal Process. Lett. 30 (2023) 1242–1246.
[23] J. Liu, Y. Li, C. Gu, Solving phase ambiguity in interferometric displacement measurement with millimeter-wave FMCW radar sensors, IEEE Sensors J. 22 (9) (2022) 8482–8489.
[24] B. Liu, L. Wu, X. Song, H. Hao, L. Zou, Y. Lu, Punet: A robust framework for phase unwrapping in interferometric SAR, Front. Environ. Sci. 11 (2023).
[25] M. Scherhäufl, F. Hammer, M. Pichler-Scheder, C. Kastl, A. Stelzer, Radar distance measurement with viterbi algorithm to resolve phase ambiguity, IEEE Trans. Microw. Theory Tech. 68 (9) (2020) 3784–3793.
[26] S. Vijay Kumar, X. Sun, Z. Wang, R. Goldsbury, I. Cheng, A U-net approach for InSAR phase unwrapping and denoising, Remote. Sens. 15 (21) (2023).
[27] L. Zhang, G. Huang, Y. Li, S. Yang, L. Lu, W. Huo, A robust InSAR phase unwrapping method via improving the pix2pix network, Remote. Sens. 15 (19) (2023).
[28] W. Xu, Y. Li, C. Gu, J.-F. Mao, Large displacement motion interferometry with modified differentiate and cross-multiply technique, IEEE Trans. Microw. Theory Tech. 69 (11) (2021) 4879–4890.
[29] Z. Ma, J. Choi, H. Sohn, Continuous bridge displacement estimation using millimeter-wave radar, strain gauge and accelerometer, Mech. Syst. Signal Process. vol. 197 (2023) 110408.
[30] G. Guerzoni, E. Faghand, G.M. Vitetta, L. Vincenzi, E. Mehrshahi, Novel movement-based methods for the calibration of colocated multiple-input multiple-output radars, IEEE Access 11 (2023) 116090–116108.
[31] S.M. Patole, M. Torlak, D. Wang, M. Ali, Automotive radars: A review of signal processing techniques, IEEE Signal Process. Mag. 34 (2) (2017) 22–35.
[32] G. Zhang, Y. Wu, W. Zhao, J. Zhang, Radar-based multipoint displacement measurements of a 1200-m-long suspension bridge, ISPRS J. Photogramm. Remote Sens. 167 (2020) 71–84.
[33] M. Planitz, Inconsistent systems of linear equations, Math. Gaz. 63 (425) (1979) 181–185.
[34] Texas Instruments, Design guide: TIDEP-01012; Imaging Radar Using Cascaded mmWave Sensor Reference Design, 2019, Available at https://www.ti.com/lit/ug/tiduen5a/tiduen5a.pdf.
[35] R. Guidorzi, R. Diversi, L. Vincenzi, C. Mazzotti, V. Simioli, Structural monitoring of a tower by means of MEMS-based sensing and enhanced autoregressive models, Eur. J. Control 20 (1) (2014) 4–13.
[36] H.S. Lee, Y.H. Hong, H.W. Park, Design of an FIR filter for the displacement reconstruction using measured acceleration in low-frequency dominant structures, Internat. J. Numer. Methods Engrg. 82 (4) (2010) 403–434.